A System for Near-Real-Time Monitoring of the Sea State Using SAR Satellites

Andrey Pleskachevsky, Björn Tings, Sven Jacobsen, Stefan Wiehle, Egbert Schwarz, and Detmar Krause

***Abstract*— This article introduces an improved system for sea state observations for near-real-time (NRT) services using satellite-borne synthetic aperture radar (SAR). The empirical algorithm SAR sea state retrieval (SAR-SeaStaR) applies a combination of a classical approach using linear regression (LR) with machine learning (ML). SAR-SeaStaR includes a series of filtering and control procedures and a series of LR and ML model functions for different satellites/modes and following integrated sea state parameters: total significant wave height H_s, wave heights of dominant and secondary swells and windsea, mean, first and second moment wave periods T_{m2}, and windsea period. SAR scenes are processed in raster format, the output are fields for each parameter showing their spatial distribution. In the scope of this study, the ML models were developed for H_s and T_{m2} and implemented into SAR-SeaStaR for processing Level-1 (L1) products of X-band TerraSAR-X (TS-X) StripMap (SM) and C-band Sentinel-1 (S1) interferometric wide swath mode (IW), S1 extra wide (EW). The validations are based on processing large worldwide archives with several years of acquisitions. Hindcast data from numerical spectral models and in situ buoys measurements are used as ground truth. The root mean squared errors of the complete system reached from these archived data for H_s are RMSE = 0.35 m for TS-X SM (pixel spacing ca. 1.2–4.5 m pixel), RMSE = 0.25 m for S1 Wave Mode (WV), (ca. 3.5 m pixels), RMSE = 0.42 m for the coarser S1 IW (10 m pixels) and RMSE = 0.52 m for S1 EW (40 m pixels). SAR-SeaStaR was implemented in the sea state processor (SSP) software using modular architecture and applied at the DLR ground station (GS) in Neustrelitz as part of an NRT demonstrator service. S1 IW data acquired over North and Baltic Sea are processed automatically, surface wind and sea state parameters are provided daily.**

***Index Terms*— CWAVE_EX, integrated sea state parameters, linear regression (LR), machine learning (ML), near-real-time (NRT) processing, synthetic aperture radar (SAR).**

I. Introduction

A. SAR Processing for Meteo-Marine Parameters Estimation

MOST of the international goods transportation of cargo takes place across the oceans, which increases the importance of marine surveillance throughout the world. Synthetic aperture radar (SAR) satellites are a significant component of Maritime Situational Awareness (MSA) systems, which fuse the data from various sources based on remote sensing, in situ measurements, forecast modeling, and communication systems for the safety of navigation [1]. An active sensor provides SAR the ability to derive spatial meteomarine information for wide-swath areas independent of sun illumination and cloudiness.

In terms of technology, the newest developments of space-based SAR sensors, the improved transmission of data from satellites to ground stations (GSs) and data processing infrastructures, and the latest retrieval methods with increased accuracy in recent years enable a number of near-real-time (NRT) oceanographic applications (e.g., [2], [3], [4]). The tendency is to combine individual applications and algorithms such as sea state, ship detection, and oil and ice detection (e.g., [5], [6], [7], [8]), into universal systems where the parallel processing branches can exchange information derived from the same SAR scene in order to improve accuracy of the results.

Furthermore, collocation and combination of satellites with different radar bands, altitudes, and different SAR modes offers an opportunity to compare and improve the developed methods for various SAR-based applications. This opportunity is demonstrated, for example, in [9], where the detectability of ship wake components is compared between C-band and X-band SARs, while the influence of local environmental parameters (i.e., sea state and wind) estimated from corresponding SAR scenes is taken into account. Such an approach requires the development of processing systems capable of extracting information (sea state in this study) from various satellites in NRT, and also capable of quickly re-processing large archived data with testing various processing options (filtering, denoising, rescaling, control-of-features, control-of-results) and also different model functions.

In terms of methodology, machine learning (ML) techniques took a leading position in science in the last few years, as their results are superior to empirical algorithms of the first-generation based on simple empirical functions (e.g., [10]) and methods of the second-generation based on linear regressions (LR) use wide series of SAR image features (e.g., CWAVE-family algorithms [11], [12]). ML models with higher complexity can be trained, since sufficiently large databases are available and can be quickly processed and analyzed due to higher computational power. Only a few

Manuscript received 10 November 2023; revised 11 March 2024 and 23 May 2024; accepted 9 June 2024. Date of publication 3 July 2024; date of current version 12 August 2024. *(Corresponding author: Andrey Pleskachevsky.)*

Andrey Pleskachevsky, Björn Tings, Sven Jacobsen, and Stefan Wiehle are with Maritime Safety and Security Laboratory at Bremen, German Aerospace Center DLR, Earth Observation Center, 28359 Bremen, Germany (e-mail: Andrey.Pleskachevsky@dlr.de).

Egbert Schwarz and Detmar Krause are with Maritime Safety and Security Laboratory at Neustrelitz, German Aerospace Center DLR, Earth Observation Center, 17235 Neustrelitz, Germany.

Digital Object Identifier 10.1109/TGRS.2024.3419582

years ago, a ML approach did not provide noticeably more accrue solutions compared with classical approaches. For example, in 2017, the accuracy of significant wave height H_s obtained from Sentinel-1 (S1) wave mode (WV) imagery by applying neural networks (NN) had not improved significantly the RMSE of ca. 0.50 m of the conventional CWAVE method [12]. However, in 2020, the accuracy was significantly improved to an RMSE of ca. 0.30 m [13] by using a deep learning technique. Further, in 2022, the accuracy of ca. 0.25 m was achieved by ML using support vector machine (SVM) technique applied to the same data and ground truth sources [14].

However, practical application of LR and ML models reveals that both LR and ML methods have their advantages and disadvantages. The advantage of the LR approach is the availability of an analytical solution bases on a series of coefficients that can be estimated quickly and an extensive learning process is not required. Further, despite the overall lower accuracy, LR has proven more stable extrapolating when the data are beyond training domains (e.g., rare extreme weather conditions such as storms, hurricanes, or a complex combination of wave systems and artifacts in the SAR image), while the ML models can result in an error under such conditions. Basically, the ML functions are more flexible and require larger training datasets for a robust solution. Generally, the linear solution is already stable with around 1/10 samples needed for ML by using worldwide data with normal distribution (random worldwide sea state is near-normal distributed with ca. 70% of all data in the domain 0–3 m H_s, ca. 5% of waves reach a height of 6 m, and only 0.1% exceed 10 m [14]).

Furthermore, the training time of ML model can take months. Regarding storage space, the developed ML model is many orders of magnitude larger (several gigabytes) than the list of coefficients for the LR (a few kilobytes). Parsing the ML model in a production run takes much longer than parsing the LR model. This point is especially important for NRT services for which these models are ultimately developed. Recently, a migration of the sea state processor (SSP) for direct installation on a satellite for onboard processing has been developed [15]. In this case, processed sea state parameters can be directly transferred from satellite to earth for NRT services. This technology will significantly reduce the sea state products delivery delay in comparison to today's technology based on transfer of the huge raw SAR data to a GS for subsequent processing.

Based on this background, a combination of LR and ML methods should benefit from the advantages of each method. For example, as it was shown in [14], using the LR solution as a first guess value for ML accelerates the training procedure and slightly improves the resulting RMSE by ca. 1–2 cm in terms of H_s. Further, as already mentioned, LR is less accurate, but the extrapolations are more robust. For example, as found in this work, under rare extreme storms conditions ($H_s > 8$ m), a difference between H_s estimated by ML and LR of more than 4 m indicates a failure of ML; therefore, LR can be used as a control-of-results in order to check validity of the ML solutions.

B. Objective of the Study

The purpose of this study was improving a system designed to process integrated sea state parameters from SAR imagery for NRT services. The CWAVE_EX algorithm bases on LR was developed in previous study [14] and realized in the SSP as one of the processing branches in the SAR AIS Integrated Toolbox (SAINT) package [4]. SAINT includes a series of parallel branches for processing different meteo-marine parameters and targets: sea state, oil, ships, ship wakes, surface wind, coastline, iceberg detection, sea ice classification, and drift. Information from different layers is shared with each other to improve product accuracy. For example, ship motion and background meteo-marine information retrieved from SAR scene were combined in ship detectability models to connect the probability of SAR ship detection information with the actual wind and sea state (e.g., [8], [9]). In turn, SAINT is incorporated into the NRT processing chain at DLR (German Aerospace Center) GS Neustrelitz (for more information see Section IV "Implementation").

The SSP was designed in a modular architecture for different satellite and modes: TerraSAR-X (TS-X) StripMap (SM), S1 interferometric wide swath mode (IW), S1 extra wide (EW) and S1 WV Level-1 (L1) products. At present, it utilizes the LR model functions CWAVE_EX established for estimation of eight integrated sea state parameters [14]: total significant wave height H_s, wave heights of dominant and secondary swell $H_s^{\text{swell}-1}$, $H_s^{\text{swell}-2}$, wave height of windsea $H_s^{\text{wind,}}$ mean wave period T_{m0}, first and second moment wave periods T_{m1}, T_{m2} and periods of windsea T_{wind}. The SAR scenes are processed in a raster format and result in continuous sea state fields. An exception is S1 WV where averaged meteo-marine parameters for each along-orbit imagettes of ca. 20 × 20 km are estimated.

Within the scope of this work, the new empirical model functions based on a ML approach were developed for two basic parameters H_s and T_{m2} for all satellites/modes listed above (TS-X SM, S1 IW, and S1 EW, in total six new model functions). A series of processing steps and several model functions, considered previously independent and different for various parameters and satellites are systematized, unified and combined into one universal algorithm. The proposed algorithm combines both: LR models (based on CWAVE approach [11] extended by additional features [4], [14]) and new developed ML models.

II. Methods and Data

In this study, SAR C-band data from the Copernicus S1-A and S1-B satellites and X-band data from the TS-X and TanDEM-X satellites have been used. As ground truth, two hindcast spectral models and buoy measurements were applied. As the amount of data is in the order of hundred thousand of samples, rounded values are given in the text.

A. Methodology

The empirical algorithm SAR Sea State Retrieval (SAR-SeaStaR) has been introduced in this study. It is based on combination of the LR function CWAVE_EX [14] and a ML

TABLE I
EFFECT OF THE PROCESSING STEPS TO ENTIRE ACCURACY IN TERMS OF WAVE HEIGHT RMSE. THE PERCENTAGE GIVES THE APPROXIMATE INPUT OF EACH STEP CONSIDERED SEPARATELY

Step	Process	effect on RMSE	kind of effect/ comment
1	artefacts filtering	ca.10%	individual outliers/ coastal areas
2	resampling/ denoising	ca. 20%	general, mostly sea state 1-5 m H_s
3	control-of-feature	ca.10%	general
4	implementation of model functions	ca. 30%	general/ % in comparison to CWAVE [6],
5	control-of-results	ca.10%	individual outliers/ coastal, fronts

approach using the SVM technique. The algorithm includes the complete processing chain with a series of steps needed to reach high accuracy.

1) Filtering of the image artifacts (e.g., ships, wakes, offshore windfarms constructions).
2) Resampling and denoising (e.g., for S1 IW resampling from 10 to 2.5 m pixel spacing).
3) SAR features estimation and control-of-features.
4) Model functions (LR and ML models) for estimation of sea state parameters.
5) Control-of-results using filtering procedures.

Each processing step contributes to the entire accuracy of the algorithm. In scope of this study, a series of tests with switching individual steps were carried out and the effect of each step was evaluated (see Table I). The rounded numbers are valid for all considered satellites/modes. It can be clearly seen that the cumulative impact of the preparation of the subscenes and control procedures has an effect comparable to the effect of the model function. For these reasons, all of these steps were committed to model functions within the algorithm.

Steps 1–3 are described in [3] and [4] in detail. Detailed information on step-5 (control-of-results procedure) can be found in [14]. The focus of this study is step-4 which includes the model functions and their development. A series of LR of CWAVE_EX model functions were developed for each satellite/mode and each sea state parameter in [14]. Analogous to [14], where MLs for S1 WV were trained, the present study focuses on the development of the new ML functions for H_s and T_{m2} for TS-X SM, S1 IW, and S1 EW. These for two parameters are commonly used for general characterization of the sea state and are provided by majority of the buoys. In our previous work [14], the SVM technique allowed improving the accuracy from ca. 35 cm, reached with CWAVE_EX method, to ca. 25 cm.

Due to the combination of LR and ML methods, the SAR-SeaStaR algorithm includes both.

1) CWAVE_EX functions (32 functions: eight parameters × four satellite modes).
2) SVM models (currently eight functions: two parameters × four satellite modes).

Actually, when processing SAR scenes:

1) Six parameters are only derived by CWAVE_EX [14].
2) H_s and T_{m2} have both CWAVE_EX and an improved SVM ML solution.

Compared to [14], where SVM for S1 WV was applied as a postprocessing operation, in the current work, all SVM models are incorporated into one processing chain of SSP and are directly executed as part of the NRT processing. However, the use of the additional SVM processing is optional. It can be skipped if timeliness is preferred over result quality. The complete workflow of the SAR-SeaStaR can be seen in Appendix.

B. Sea State Parameters Estimation

The estimation of sea state parameters bases on an analysis of the normalized radar cross section (NRCS) of a subscene. A series of subscenes are initialized in a raster format and their analysis results in a continuous sea state field for series of integrated parameters. The raster step is the distance between the center points of analyzed subscenes. It was experimentally found out that for optimal control-of-features (by comparison with the neighboring subscenes) a raster step between 1/4 and twice the subscene size should be chosen [14].

One of the basic variables represents the SAR image spectrum obtained using fast Fourier transformation (FFT) applied to radiometrically calibrated, filtered, denoised, land-masked, and normalized subscenes with a size of 1024 × 1024 pixels in wavenumber k domain as introduced by Pleskachevsky et al. [4]. The primary SAR features estimated from a subscene are of five different types.

1) NRCS and NRCS statistics (variance, skewness, kurtosis, etc.), in total nine features.
2) Geophysical parameters (surface wind speed estimated from analyzed subscene using CMOD-5 algorithms for C-band [16] and XMOD-2 for X-Band [17]), one feature.
3) Gray level co-occurrence matrix (GLCM) parameters (homogeneity, dissimilarity, etc.), in total eight features.
4) Spectral parameters based on image spectrum integration for different wavelength domains (0–30 m, 30–100 m, 100–400 m, etc.) and spectral width parameters (Longuet–Higgins, Goda), in total 17 features.
5) Spectral parameters using products of normalized image spectrum with orthonormal functions (CWAVE approach) and *cutoff* wavelength estimated using autocorrelation function (ACF), in total 21 features.

Note, both sea state and wind are estimated from prefiltered subscenes, and there the NRCS outliers (ships, wakes, oil, etc.) and noise are essentially removed.

The detailed description of all features can be found in [4] and [14]. In total, 54 primary and the 77 most significant secondary features are applied in CWAVE_EX. Secondary features are combinations of primary features in quadratic and inverse forms. The features normalization using the mean (MEAN) and standard deviation (STD) for each feature was

found to be optimal [14]. Each additional SAR feature slightly improves the resulting H_s RMSE by 0.1–3.0 cm with an accumulative improvement of around 15 cm in comparison to the RMSE reached in [12]. The input for the SVM functions are primary features complemented with

1) First-guess H_s from CWAVE_EX LR solution.
2) Precise incidence angle with an accuracy of third decimal place (affects the results ca. 2 cm RMSE [14]).
3) Flag identifying the satellite (S1-A or S1-B for Sentinel-1 and TS-X or TD-X for TerraSAR-X).
4) Pixel spacing (different for, e.g., TS-X SM radiometric enhanced (RE) and spatially enhanced (SE) products)
5) Flag identifying polarization (HH or VV).

In a series of several analyses used for the control-of-results [14], one of the most acting features is the so-called "Rosenthal parameter," named after Wolfgang Rosenthal (RIP 2016), who suggested its introduction. The Rosenthal parameter E_R indicates an integration of the image spectrum with an additional scaling of $1/k$ for each spectrum bin. In contrast to a direct integration, the E_R integration significantly amplifies the longer wavelength signals in the image spectrum. Objects such as ships or ship wakes significantly increase the value of E_R and, hence, can be filtered out. For each satellite/mode, the threshold value of E_R was experimentally established using statistics of processed scenes indicating the validity of the subscene for sea state estimation [14].

According to their influence on the results, the features can be systematized as follows.

1) Basic features build a stable basis for estimations. Such features [11] include parameters resulting by integration of the image spectrum and surface wind U_{10}. Using these features allows a stable estimation of the sea state parameters with a coarse accuracy regarding today's state-of-the-art (first-guess solution). The impact of each feature is in range of centimeters in terms of H_s RMSE.
2) Additional features allow improving RMSE gained using basic features. These are a series of features each contributing to the RMSE improvement in the order of millimeters, but the combined total contribution of all additional features is in the range of centimeters. These features include, for example, GLCM-based features.
3) Features dealing with rare conditions and not contributing to the total RMSE. These features deal with individual outliers such as strong storms, zero-wind, or scenes with many artifacts (e.g., ships or algae spots). For example, the feature INT ensures correct estimation of enormously high waves. INT means integration of the weighted Complementary Cumulative Distribution Function (CCDF) of the pixel's brightness and has pronounced high values only for individual high waves above ca. 10 m·
4) Control features used for assessment the validity of the subscene and results. An example of such a feature is E_r.

C. Model Function and Its Application

In continuation to study [14], the SVM technique was applied. The nu-SVR Support Vector Regression (ν-SVR) [18] with a radial basis function as kernel type was chosen as the most suitable for the used features and ground truth as a result from testing several different hyperparameter setting with different kernel functions [14]. For practical applications, the high-performance ThunderSVM (TSVM) library was applied [19]. TSVM runs an order of magnitude faster than the standard LibSVM and allows training of large datasets with millions of samples for all 59 SAR features used in this study.

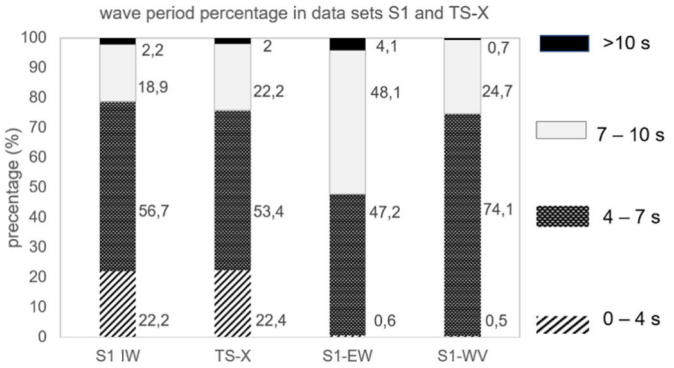

Fig. 1. Percentage of the T_{m2} wave period in global S1 and TS-X datasets. Due to acquisitions of TS-X and S1 IW in coastal areas, the percentage of very short waves with period under 4 s is quite high with ca. 22% of all data.

The main difference between S1 WV data trained in study [14] and the current study was a switch to acquisition areas with other geophysical conditions, while S1 WV are acquired only in open ocean, S1 IW and TS-X SM are acquired predominantly in coastal waters and closed seas. Ice-free S1 EW were dominantly acquired in open ocean in areas with pronounced storms (ca. 70% in North Atlantic). The consequence is a significant increase of artifacts (ships, wakes, offshore constructions, oil spills etc.) and a larger percentage of short waves with wavelengths below *cutoff* in S1 IW and TS-X SM. Additionally, in coastal shallow waters, where the bathymetry plays a role, the model ground truth has stronger uncertainties due to differences in model space resolutions and bathymetry.

Fig. 1 shows the statistics for the T_{m2} period for all datasets. It represents the sea state distribution for short and long wavelengths. Due to the acquisitions of TS-X and S1 IW in coastal areas, the percentage of very short waves with periods under 4 s (means wavelength in order ca. $<$50 m) is quite high with ca. 22% of all data. As sea state much shorter than *cut off* enters the SAR image predominantly as noise, it needs special consideration when achieving high accuracy for all period (i.e., wavelength) domains.

As the algorithms are developed for practical daily NRT use, special attention was paid to stability and applicability of the algorithm under all conditions (also for low wind under 1.5 m· s^{-1}, which previously was excluded as not physically trustworthy in [14]) and areas (e.g., coastal waters, harbors). In this way, the model functions were especially trained for all data without prefiltering nonvalid scenes by using, for example, homogeneity test by variance [12]. Although this precondition introduces additional difficulty into trainings, the resulting model functions are able process all scenes except only ca. 0.1% of subscenes, which are detected as

"non-valid" (acquired directly over strong artifacts such as multiple ships, oil spills, which were not able to be removed from the subscene due to their configuration or size during the subscene-preparation processing step). In comparison, the accuracy in [14] for S1 WV was achieved with ca. 2% detected "nonvalid" subscenes even for open ocean acquisitions.

A series of sensitivity tests was carried out for S1 IW, S1 EW, and TS-X in this study in order to verify the applicability of the SVR hyperparameters found to be optimal for S1 WV during previous study [14].

The trainings and validations were repeated using a series of cost regularization parameters C {25–100} and exponential degrees in the radial basis function γ ={0.001–0.010} analogous to [13] for both H_s and T_{m2}.

In terms of H_s, it was found that for the mentioned satellite/modes, using stronger $\gamma = 0.01$ extends the training time by a factor of about five in comparison to γ =0.001, while the resulting accuracy is improved by ca. 3 cm.

In terms of the period T_{m2}, the same changing of γ results into a training time around ten times longer with an comparable effect on accuracy.

Generally, it was found that the wave period trainings need more effort and time than the wave heights (more details and summaries on period training see Section III-A). It also became obvious that training the dataset including a higher percentage of waves with short wavelength also requires more training time using the same SVM hyperparameters.

A series of model functions with different hyperparameters were collected. For archive processing (see Section III-B), the function with optimal hyperparameters were chosen.

1) The cost regularization parameter $C = 55$.
2) The exponential degree in the radial basis function $\gamma =$ 0.0075 (gamma).
3) The parameter ν (nu) determines the proportion of the number of support vectors to keep in the solution with respect to the total number of samples in the dataset ($0 \leq \nu \leq 1$, $\nu = 0.5$ was implemented).
4) Tolerance of the termination criterion defines how close the compared models should be reached by the next iteration $e = 0.01$.

The technical realization of the algorithm in the SSP software-packet using modular architecture allows to switch SVM functions to a more modern one when expanding the number of training events, or disable it. In this case, the processor gives the results only using LR CWAWE_EX (see Fig. 11).

D. Training and Validation Procedures

The fundamental difference between TS-X and S1 satellites is the availability of data. In contrast to S1 satellites, for which the data are acquired daily worldwide in an automatic way and the ESA archive allows a routinely downloading thousands of scenes, TS-X acquisitions over ocean are rare. Each TS-X image was individually ordered by a user. Downloading of TS-X is also individual for each scene, not all archived scenes are available for the scientific use. In this way, the following approach was used:

1) For S1, all initially in [14] collected data were divided into training and validation sets (ca. 70% and 30% correspondingly). During the training, new data were downloaded from ESA datahub and processed. This training dataset extension was repeated until the next independent validation measured improved the RMSE, while individual storms were reproduced.
2) For TS-X, all scenes acquired over ocean, which can be accessed via the TS-X science archive were collected for 2009–2022 (ca. 60% of all existing TS-X SM acquisitions over oceans available for scientific studies). Again, these were divided into training (analogically ca. 70%) and validation datasets.

The main problem of improving the model was the insufficient number of cases with wave height higher than 6 m H_s (see sea state statistics in Table III). Around 70% of all data are waves in the domain 0–3 m H_s, and the number of samples collected in scope of [14] for this domain was already sufficient at the beginning of this study. With ML training, a linear increase of data leads to an exponential increase in training time. For instance, by H_s training, the doubling of the data from for example, 0.5 to 1 Mio samples increases the training time by ca. seven times when using the same number of parallel running CPUs. In order to accelerate and improve the learning, the data were divided into domains according to H_s (see values in Table III) and recombined. In this way, the training dataset was supplemented foremost with data for domains reflecting storms. All new data not used in the training were included in the validation sets.

E. SAR Data

For S1, the original Ground Range Detected (GRD) IW and EW L1 products are used in this study. The scenes are available in single (HH or VV) or dual (HH + HV or VV + VH) polarization. For sea state estimation, the VV or HH polarization data were used, with priority given to VV products.

For TS-X, SM L1 multi-look ground range detected (MGD) standard products are used. From the S1 and TS-X archives, only scenes with ocean at least 5 km off the coast were taken into consideration by training and validations. Generally, only the data in ice-free regions $-55°$ <latitude $<60°$ were considered.

For S1 IW, around 6000 S1 IW individual images were collected for years 2016–2022. The data include worldwide acquisitions including North Atlantic, west and east coasts of USA and Canada, Japan, Australia, Aleutian Islands and Hawaii, Mediterranean, North, Baltic, and Black Seas. Special attention was given to including scenes of severe storms, cyclones, and hurricanes (e.g., hurricane Irma in 2017, [20]). Each IW image covers an area of around 250 km × 200 km. The S1 IW scenes were processed with a 10 km raster with around 500 samples per image. However, in coastal areas, the relatively coarse grid resolution of the ground truth wave models requires an additional distance of around 10 km from the coastline. In total, ca. 2 Mio samples collocated with ground truth were collected.

After a series of tests with different setups [4], [14], a denoising operation was employed which significantly improves the results for modes with coarse resolution. For an initial subscene of 256 × 256 pixels (covers an area of 2560 m × 2560 m in S1 IW with 10 m original pixel spacing and 10 240 × 10 240 m in EW with 40 m pixels, both GRD products), a resampling with a factor of four (each pixel is divided into 4 × 4 = 16 pixels with the same NRCS value and with a size of 1/4 of the original spacing) followed by 2-D Gaussian smoothing has been applied. The resulting 1024 × 1024 pixels subscene further applied for FFT analysis has a modified pixel resolution of 2.5 m for IW and 10 m for EW. Due to this operation, the wave-like structures associated with sea state and the corresponding peaks in the image spectrum are stronger pronounced.

S1 EW images are mostly acquired in Polar Regions where sea ice is present (ca. 80% all acquisitions). However, a number of S1 EW images were acquired in ice-free regions and around the equator and other areas (e.g., Madagascar). For this study, almost all EW archived images for 2016–2022 in ice-free regions were collected. The processing with a raster of 20 km resulted in around 400 collocated samples per individual EW image covers each ca. 400 km × 400 km. In total, around 2500 S1 EW images were collected and resulted in around 1.2 Mio samples collocated with model.

TS-X SM. For this study, worldwide archived TS-X SM data acquired over ocean with ca. 7000 scenes were collected. The TS-X SM images were acquired either in single polarization (VV, HH) or dual polarization (VV + HH). Around 30% of all pooled TS-X SM data had dual polarization. Here, both polarizations were used individually, extending the number of samples for each polarization. Each TS-X SM scene covers an area of ca. 30 km × 50 km. The subscene size for TS-X SM is different with coverage of ca. 3.7–4.6 km dependent on the pixel spacing of the TS-X SM RE products (1.2–4.5 m). Since TS-X SM scenes are often acquired near the coast and over harbors, around 60% of all processed subscenes cover land and only around 40% covers sea surface and could be used for the ocean collocations. Processed with a raster step of 1.5 km, the collected TS-X SM images resulted in around 1.5 Mio collocated model samples.

F. Ground Truth Data

In this study, two kinds of ground truth were used: numerical hindcasts covering worldwide sea state, and local in situ measurements from wave rider buoys. The spectral integrated parameters from two hindcast wave models were employed:

1) Météo-France WAve Model (MFWAM) [21]. MFWAM results are available with a spatial resolution of 1/12° (available from 2016 onward [22]).
2) WaveWatch-3 (WW3) model of National Oceanic and Atmospheric Administration (NOAA, [23]) with a spatial resolution of 1/2° (spatially interpolated for collocation) for collocations before 2016. Further, T_{m1} wave period was provided only by WW3.

The model results are provided in 3-h steps and are temporally interpolated.

For collocations before 2016, it was found that sea state is extrapolated toward the coast in WW3 data with coarse resolution, while in the fine resolution MFWAM model (and corresponding SAR subscenes) the sea state is already dissipated. An additional MFWAM land mask with 1/12° resolution was generated and applied to WW3 results in order to avoid overestimated ground truth wave height in the subscenes next to the coastline. This operation reduces the model ground truth uncertainty and helps to significantly improve the training for near-coast sea state.

As an independent validations source, the observations from in situ buoys were used, provided from different operators with focus on National Data Buoy Center (NDBC), Environment and Climate Change Canada (ECCC) and European Marine Observation and Data Network (EMODNET) [24], [25], [26]. For a statistically significant validation, these buoy measurements provide a sufficient collocation density in the order of thousand samples for S1 IW, while for S1 EW and TS-X collocations can be found only for individual cases.

The uncertainty in the ground truth was evaluated around 0.25 m for H_s, as the H_s comparison for models and NDBC buoys resulted in an RMSE = 0.26 m for MFWAM/NDBC and RMSE = 0.23 m for MFWAM/WW3 at NDBC buoy locations [14].

G. Additional Correction and Filtering Procedures

The model functions for sea state parameters were developed and implemented for processing each parameter independently. However, since the parameters are defined as results of the integration of the same wave spectrum, they are related. In this study, a series of corrections of the resulting sea state parameters were introduced (see Table I) by connecting the parameters based on physics and statistics. This step plays a greater role, the more data are processed. Regardless of the quality of the functions, when processing a large amount of remote sensing data, the appearance of individual outliers is inevitable; the challenge is to properly handle these outliers.

Using H_s, the most stable parameter, trained with ML, a series of thresholds were introduced using the definition of the parameters for partial integrated parameters (CWAVE_EX):

$H_s > H_s^{\text{swell}-1} > H_s^{\text{swell}-2}, H_s > H_s^{\text{wind}}$. In this way, the swell and windsea outlier values are accordingly reduced.

The wave energy balance was taken into consideration by estimating the significant wave height using three components $(H_s^{\text{swell}-12} + H_s^{\text{swell}-22} + H_s^{\text{wind2}})^{0.5}$. The comparison with H_s estimated by model functions allows compensating the energy deficit by modifying $H_s^{\text{swell}-2}$ (which generally has lower values with ca. 0.68 m for S1 IW datasets (dominant swell ca. 2.14 m) and is the weakest component in terms of accuracy due to uncertainties in ground truth by partitioning of the wave spectrum into dominant and secondary wave systems).

The NDBC measurements were analyzed for a relationship between wave period and wave height. From the point of view of physics, these parameters are independent. In nature, however, due to the parameters of the medium (i.e., water surface tension), they interact closely. In fact, large wave

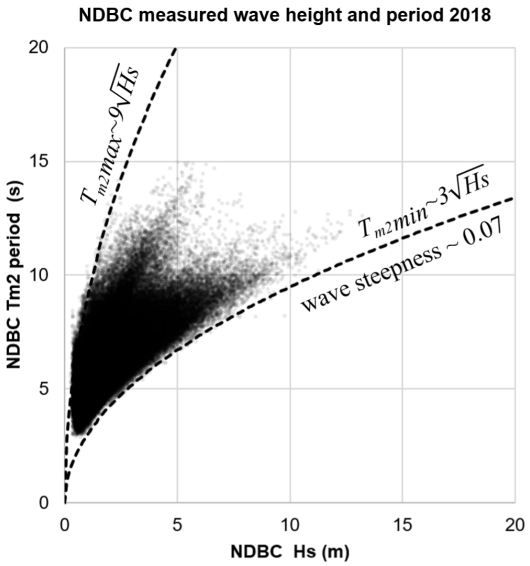

Fig. 2. Measured significant wave height H_s and T_{m2} wave period from 70 worldwide NDBC buoys in 2018 with ca. 1.5 Mio samples. The enveloping min and max curves are applied as low and high pass filters for the periods estimated from SAR using processed H_s.

heights cause longer wave periods: waves with short periods mean shorter wavelengths L and accordingly stronger wave steepness, which leads to wave breaking. Fig. 2 presents the worldwide measurements from 70 NDBC buoys for 2018 with ca. 1.5 Mio samples, H_s and T_{m2} are plotted against each other and the min and max enveloping curves were approximated. Based on this statistic, the corresponding min and max enveloping functions for T_{m2} were applied

$$T_{m2}^{\min} = A_{\min}\sqrt{H_s}, T_{m2}^{\max} = A_{\max}\sqrt{H_s} \quad (1)$$

with $A_{\min} = 3$ and $A_{\max} = 9$. The corresponding filter reset the T_{m2} outliers corresponding to these functions in the control-of-results block. By applying the deep-water dispersion relation for estimating the corresponding wavelength ($L = gT^2/2\pi$), this corresponds for min to a maximal wave steepness of 0.07 ($H_s/L \sim 1/14$) and for max to a minimal steepness of 0.008 ($H_s/L \sim 1/125$). The main condition for wave breaking is the exceeding of the local orbital velocity U_{orb} in wave crests the phase velocity c_p of a wave crest propagation. A rough assessment of deep-water c_p based on period and wavelength and maximal U_{orb} based on wave amplitude and period results in positive values of $c_p - U_{\text{orb}}$ for $A_{\min} > 3$ and in negative values for $A_{\min} < 3$ (wave breaking condition).

Similar to wave height, based on T_{m2}, the thresholds for the periods were introduced with $T_{m2} > T_{\text{wind}}$ and $T_{m0} > T_{m1} > T_{m2}$.

The large statistics generated by archive processing has shown that worldwide $H_s > 6$ m does not occur in the open ocean under weak winds below 5 m $\cdot$ s^{-1} (with exceptions in coastal areas with beaches, such as individual solitons appearing by the coasts of Hawaii). This means that basically swell waves stay below $H_s \sim 6$ m without wind support. The higher wave heights depict a combination of swell with windsea and strong local wind. A filter was implemented to detect such individual cases as outliers.

Another phenomenon associated with trainings of machine-learning models became apparent while validating large datasets. As found in [14], the LR is less accurate than SVM, but the extrapolations are more robust. It was found in this study that under rare extreme storm conditions with $H_s >$ 8 m, in individual cases a difference between H_s estimated by ML and LR of more than 4 m indicates a failure of SVM ML (outlier). Thus, the CWAVE_EX solution was implemented to control the results in order to check the validity of the ML solutions, the H_s will reset to CWAVE_EX for such cases.

III. Results

A. Results for Total Integrated Sea State Parameters for S1 and TS-X

After a series of trainings and validations (see Section II), six new SVM models were created (SVM models for S1 WV were already developed in [14] and only incorporated into the processing chain in this study). Table II presents the overview of the resulting RMSE for all eight parameters for all considered satellites/modes by comparison of the MFWAM model results. For H_s and T_{m2}, the values in bold depict the new SVM results (only used for these two parameters) while unmarked values mean the LR CWAVE_EX [14], which is also given for the remaining six parameters. In general, the SVM solution yields a ca. 10% higher accuracy than the LR solution of CWAVE_EX in comparison with [14].

It is important to point out that the results in Table II reflect the full processing of the SAR-SeaStaR algorithm implemented in the SSP using the model functions and all steps listed in Section II-A. Applying only the model functions without any other steps statistically results in an accuracy loss of at least 15%. The corresponding validation scatter plots for TS-X SM and S1 EW are presented in Fig. 12 in Appendix. Scatterplots for S1 IW, which are additionally validated when processing long archive dataset, are shown separately in Section III-B.

Note that much more data were processed in this study in comparison to [14], including several thousands of worldwide scenes from the S1 and TS-X archives. Hence, the CWAVE_EX results slightly differ for individual parameters from the results in [14], which was, from today's point of view, based on a limited dataset.

S1 IW has better resolution and potentially can better image waves in comparison to S1 EW. Most of the S1 IW acquisitions are in coastal areas with low and short waves and with a high number of image artifacts (ships, wakes, buoys, sandbanks, etc.). Statistically, ca. 15% of S1 IW and ca. 30% of TS-X samples in this study have a near-zero wind speed under 2 m$\cdot$ s^{-1} (e.g. in areas with regions shadowed by coastal mountains in the Adriatic and Ionian Seas). The resulting low waves, usually below 0.5 m and waves with wavelengths under the so-called *cut-off* wavelength, are imaged in the form of noise in SAR image. From such noisy images (image spectrum depicts no peaks associated with waves), the wave height can quite accurately be estimated. The wave height then remains within a small domain of 0–1 m. However, low sea

TABLE II
RMSE FOR TOTAL INTEGRATED SEA STATE PARAMETERS ESTIMATED USING SAR-SEASTAR ALGORITHM FOR H_s AND T_{m2}, CWAVE_EX RESULTS [14] ARE SUPPLEMENTED BY SVM RESULTS OF THIS STUDY IN BOLD

Parameter	Unit	Satellite mode			
		S1 IW	S1 EW	S1 WV (wv1/wv2)	TS-X SM
H_s	m	**0.42** 0.57	**0.51** 0.61	0.24 / 0.28 0.34 / 0.38	**0.35** 0.42
T_{m2}	s	**0.88** 0.92	**0.69** 0.86	0.46 / 0.51	**0.45** 0.51
T_{m1}	s	0.97	0.85	0.51 / 0.56	0.59
T_{m0}	s	0.96	0.86	0.46 / 0.51	0.72
$H_s^{\text{swell-1}}$	m	0.68	0.63	0.42 / 0.47	0.33
$H_s^{\text{swel-2}}$	m	0.38	0.44	0.41 / 0.46	0.27
H_s^{wind}	m	0.77	0.66	0.40 / 0.46	0.37
T^{wind}	s	0.97	0.95	0.62 / 0.67	0.71

TABLE III
DISTRIBUTION OF RMSE FOR SIGNIFICANT WAVE HEIGHT H_s FOR S1 IW ARCHIVE 2020–2021

Sea state Domains (m)	H_s RMSE (m)		H_s BIAS (m)		N of collocations		% distribution	
	model	buoys	model	buoys	model	buoys	model	buoys
$0.0 < H_s < 1.5$	0.313	0.405	-0.155	-0.220	6,414,737	21,859	46.21	50.97
$1.5 < H_s < 3.0$	0.376	0.440	0.025	0.016	5,106,332	14,766	36.78	34.43
$3.0 < H_s < 6.0$	0.626	0.716	0.225	0.311	2,143,384	5,886	15.44	13.72
$6.0 < H_s$	1.139	1.600	0.575	1.098	217,290	375	1.57	0.87
TOTAL	0.422	0.493	-0.019	-0.054	13,881,743	42,886	100.00	100.00

state is difficult for estimating the wave period, which can differ from 1 s (very low wind sea) to ca. 15 s (long swell) for the same low wave height. Although the value of the wave period for such small waves has no practical importance (e.g., for shipping), a large number of such cases negatively affects the overall statistics. On the other hand, S1 EW are acquired in the open ocean, where swell waves dominate and can be well imaged in SAR. The number of image artifacts in S1 EW is also noticeably lower due to the open ocean areas.

It should also be mentioned that although training for H_s and T_{m2} are based on the same features and the domains for both parameters are nearly identical (0–16 m for H_s and 0–16 s for T_{m2}), the training for T_{m2} using the same number of samples takes twice the time compared to H_s trainings. The reason is the effect described above: large areas have near-zero wave heights which can be easily trained, which, however, can have a wide range of wave periods.

B. S1 IW Detailed Validation in Scope of ESA SARWAVE

An especially detailed validation for S1 IW was carried out in scope of study for the ESA SARWAVE project [27], where a large proportion of S1 IW archive over ocean for 2020 and 2021 was processed with a 5 km raster step. The ESA SARWAVE project aimed to develop methodologies for deriving sea state related parameters and wave spectra from S1 SAR IW imagery using the newest methodologies in connection with altimeter and optical sensors. In the scope of this study, DLR processed the S1 IW ESA archive for Areas-of-Interest (AoIs) cover the majority of measurement buoys open for scientific studies, that is, NDBC/ECCC around USA and Canada and EMODNET in European waters. Fig. 3 gives an overview on buoys used for validation (top) and overview of S1 IW scenes in 2020 (11 589 images) processed and validated (bottom).

H_s and T_{m2} were analyzed in detail and compared with the results of a wave model and buoy measurements. For ice-free areas $-55°$ <latitude<$60°$, ca. 14 Mio. Model collocations were collected. For buoy comparisons with a collocation radius of 10 km (means all processed S1 IW values are inside the collocation circle), ca. 45 000 buoy collocations were collected. In total, for wave height H_s, by comparison with MFWAM model RMSE = 0.42 m and BIAS = -0.02 m, by comparison with buoys RMSE = 0.49 m and BIAS = -0.05 m were reached. More detailed information on RMSE distribution for different sea state domains and as well as percental distribution of data can be found in Tables III and IV.

Fig. 4 presents scatterplots for the validation of H_s and T_{m2} against model results and buoy measurements. Fig. 5 demonstrates an example of a time series with half a year duration of H_s and T_{m2} measurements from the buoy EMODNET-1043928 (ID: 6200163) located in the North Atlantic in front of the French coast (location marked in Fig. 3) and collocated with S1 IW measurements. Fig. 6 shows an example of sea state processing for all eight sea state parameters from S1 IW scenes, covering ca. 1600 km × 200 km, acquired during a strong storm in the North Atlantic on 2020-02-14 at 18:45 UTC with H_s reaching up to 13 m. Processing in a 5 km raster results in ca. 1500 subscenes for each individual IW image. The isolines depict the results of MFWAM model at 18:00 UTC (excluding T_{m1} period which is not provided by [22]).

In Tables III and IV, the number of collocations for H_s and T_{m2} differs for both, the model and the buoys, due to two reasons:

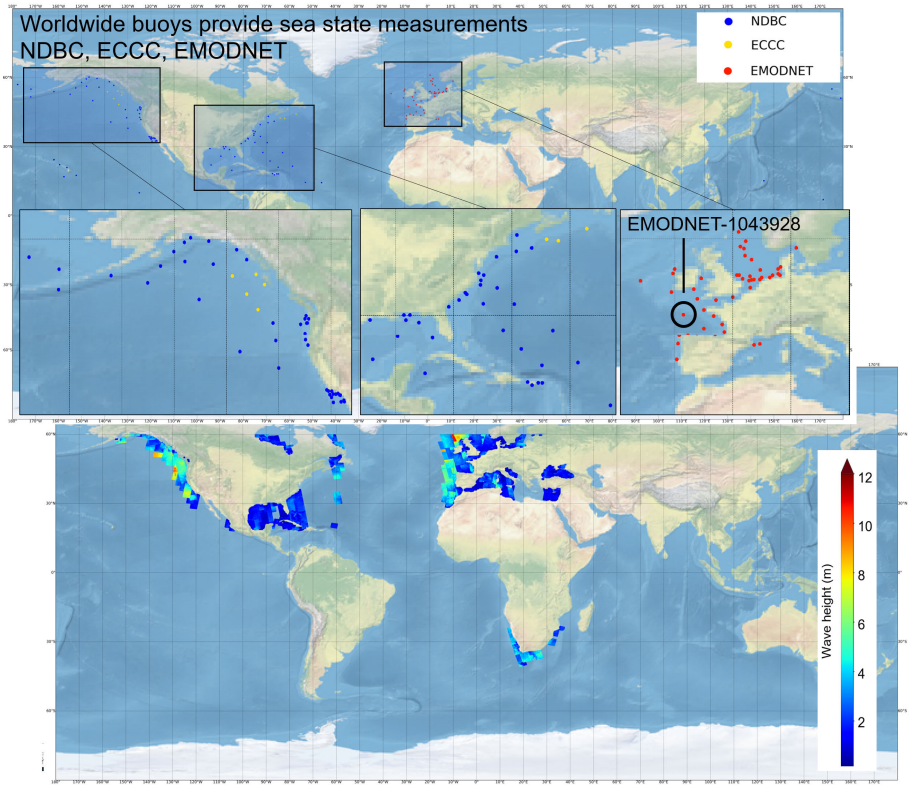

Fig. 3. (Top) Overview of buoys used in the study. (Bottom) Example coverage S1 IW in scope of the ESA SARWAVE in 2020 used for validations in ice-free area −55° <latitude<60° with total number of ca. 12 000 scenes. The scenes are displayed overlapped in the order their acquisitions, the color indicates processed wave height.

TABLE IV
DISTRIBUTION OF RMSE FOR SECOND MOMENT WAVE PERIOD T_{m2} FOR S1 IW ARCHIVE 2020–2021

Sea state Domains (s)	T_{m2} RMSE (s)		T_{m2} BIAS (s)		N of collocations		% distribution	
	model	buoys	model	buoys	model	buoys	model	buoys
$0 < T_{M2} < 4$	1.214	0.937	-1.055	-0.771	3,130,867	6,137	22.25	16.67
$4 < T_{M2} < 7$	0.618	0.773	-0.169	0.169	7,973,277	24,233	56.65	65.83
$7 < T_{M2} < 10$	0.878	1.269	0.384	0.617	2,667,261	61,48	18.95	16.70
$10 < T_{M2}$	2.102	2.816	1.654	2.275	302,710	295	2.15	0.80
TOTAL	0.886	0.934	-0.142	0.104	14,074,115	36,813	100.00	100.00

1) H_s and T_{m2} are two independent functions with their own control-of-results. For a series of certain factors (details in [14]), the resulting values can be filtered out as an error.
2) The buoy measurements have gaps in the data recording, some buoys measure only H_s.

IV. COLLOCATION OF THE RESULTS FOR DIFFERENT RADAR BANDS AND METHOD PRACTICAL IMPLEMENTATION

A. Collocation S1 IW and TS-X SM Archives

In the scope of this study, the first cross-comparison between sea state estimated from two sensors working with different radar bands and scanning modes was carried out.

The S1 IW processed scenes (complete ESA archive 2020 and 2021 for the AoI, Section III-B) were collocated to TS-X "ocean archive" (all scenes with at least 5 km water). To each S1 IW processed subscene (5 km processing raster step) several TS-X subscenes (1.5 km raster) with a distance of up to 30 km and within a ±30 min time window were assigned.

As an example, Fig. 7 shows the TS-X SM scenes from the TS-X SM ocean archive 2020 collocated with S1 IW (first row, the whole ocean archive is displayed bottom left, the color means scenes density within 20 km considering TS-X SM scene centers).

An example of a direct collocation in space and under 1 min in time acquired over Mediterranean Sea on 2020-02-03 at 05:05 UTC can be seen in the second row. In the collocated area, the wave height estimated from S1 IW is ca. 1.01 m, the averaged wave height from TS-X is ca. 0.85 m (ca. 15 cm bias for this case). The MFWAM model wave heights are ca.

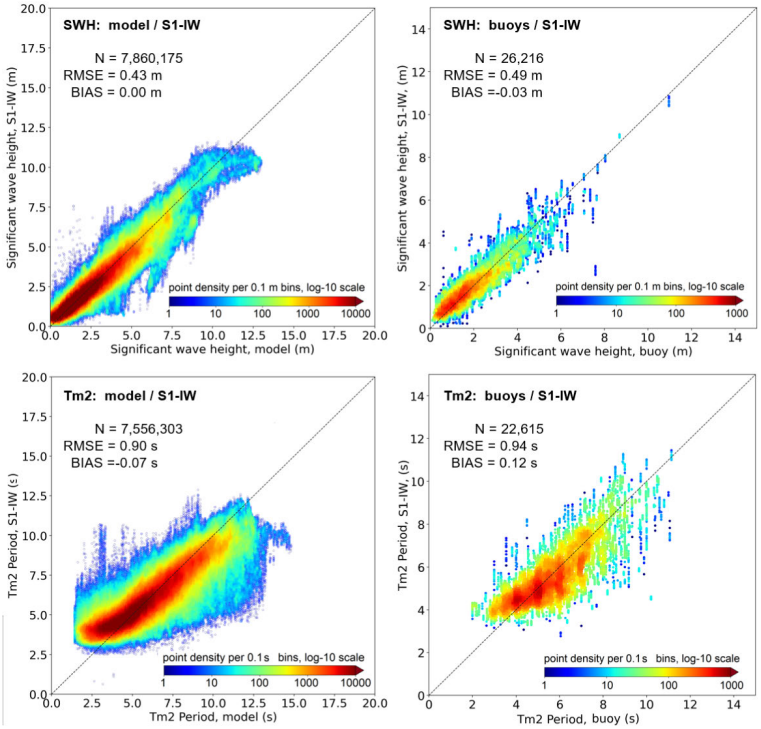

Fig. 4. Comparisons for significant wave height H_s and second moment wave period T_{m2} estimated using SAR-SeaStaR with model and buoys (10 km collocations) worldwide (see Fig. 3).

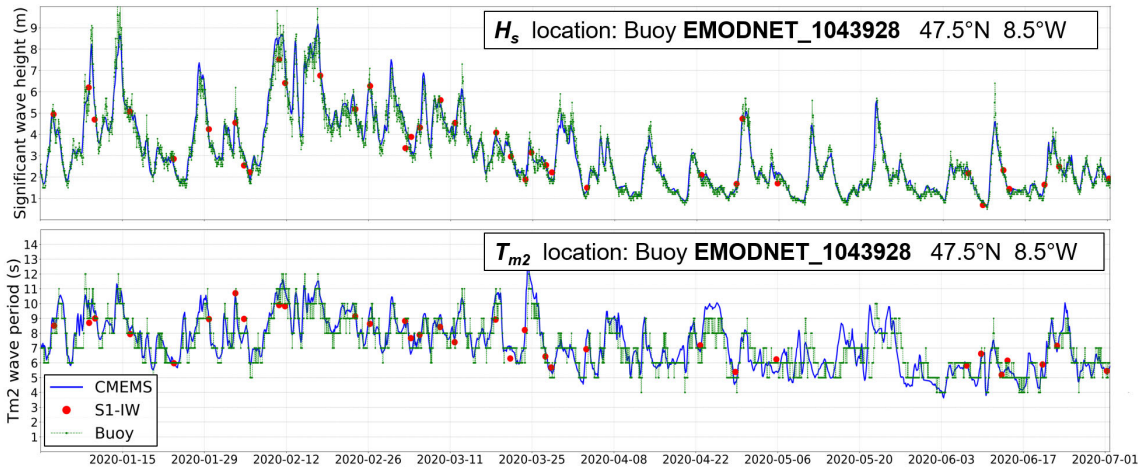

Fig. 5. Example of a time series with a duration of half a year of significant wave height H_s (top panel) and second moment wave period T_{m2}(bottom panel) for the buoy EMODNET-1043928 (ID:6200163) located in North Atlantic in front of the French coast (marked by a black circle in Fig. 3). Blue: model data, green: buoy measurement, red dots: S1 IW retrievals.

0.90 m at 03:00 UTC and increased to ca. 1 m at 06:00 UTC in the collocation area. Interpolated in time, this mean wave height of ca. 0.95 m what is exactly between these two values.

From all TS-X ocean scenes in 2020 and 2021 185 scenes could be collocated with S1 IW scenes, resulting in ca. 23 000 collocated TS-X subscenes. Fig. 8 (left) presents the statistics for time and space collocations independently, where the number of collocated images (ID products) is displayed for six domains for both time and space. The cumulative percentage is given in the vertical axis: it can be seen that only ca. 25% of all collocated S1 and TS-X are directly overlapping with a distance under 5 km, while around 50% are collocated under 10 km. In terms of time, around 50% of all collocations are under 5 min time delay.

Fig. 8 (right) presents the H_s scatterplot for collocated subscenes. A series of wave heights estimated from TS-X (1.5 km raster processing step) corresponds to one value in S1 IW (5 km step) with a distribution of the values. The statistical comparisons of H_s estimated from S1 IW and TS-X SM results in $\mathrm{RMSE}^{Hs}_{\mathrm{S1-TSX}} = 0.44$ m and $\mathrm{BIAS}^{Hs}_{\mathrm{S1-TSX}} = 0.07$ m. The numbers are on the same order as the accuracy of S1 IW compared with ground truth model data. Note, that the partial uncertainties estimated against the model only for these near-coast 23 000 locations for S1 are $\mathrm{RMSE}^{Hs,\mathrm{partial}}_{\mathrm{S1\text{-}model}} = 0.37$ m

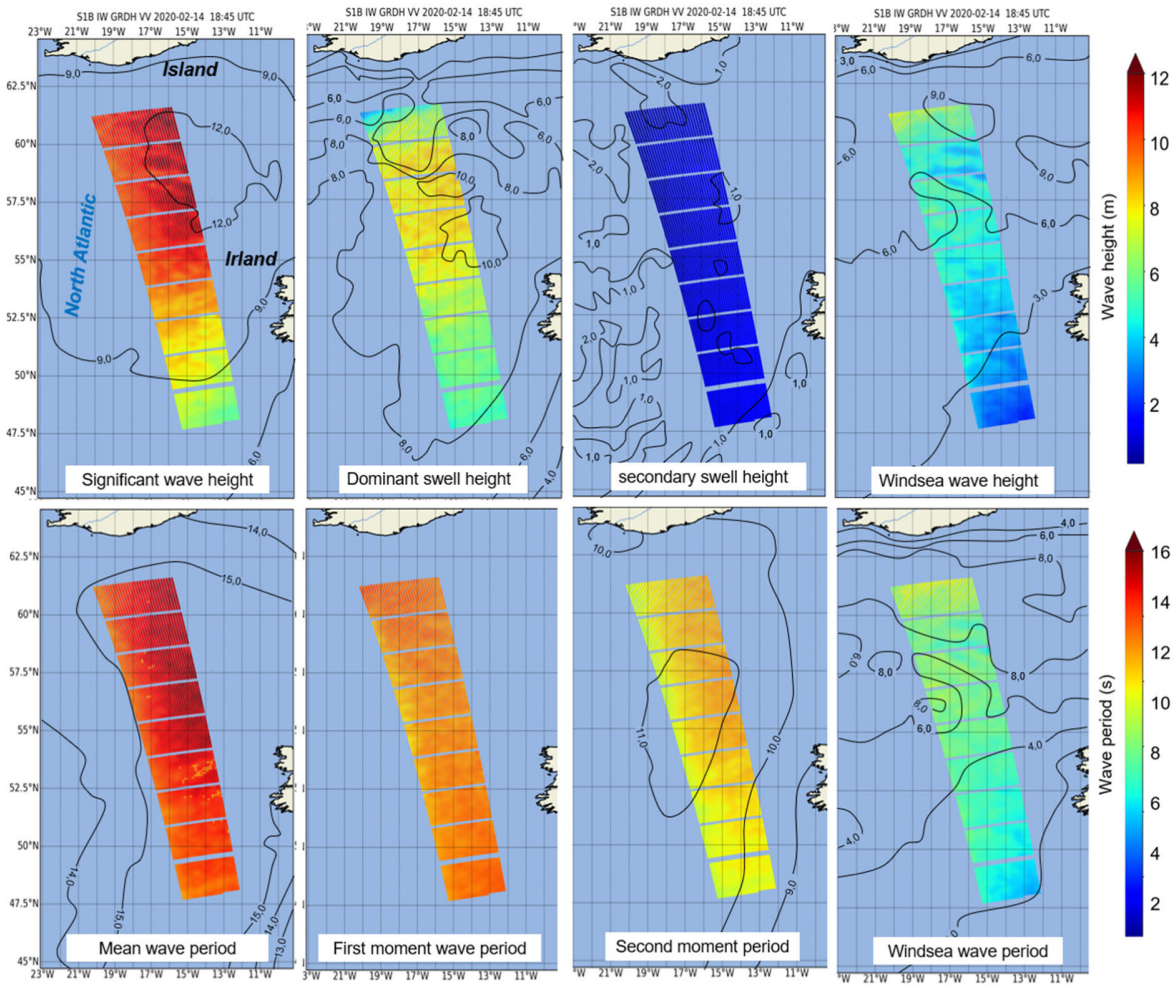

Fig. 6. Example of eight sea state fields processed from a S1 IW scene with ca. 1600 × 200 km coverage acquired during a strong storm in the North Atlantic on 2020-02-14 at 18:45 UTC with H_s reaching ca. 13 m. Processing in a 5 km raster results in ca. 1500 subscenes (approximately 30 × 50) for each individual IW image. Isolines shows the results of MFWAM at 18:00 UTC.

with $\text{BIAS}^{Hs,\text{partial}}_{\text{S1-model}} = 0.06$ m and for TS-X $\text{RMSE}^{Hs,\text{partial}}_{\text{TSX-model}} = 0.42$ m with $\text{BIAS}^{Hs,\text{partial}}_{\text{TSX-model}} = -0.01$ m. In this way, bias between S1 and TS-X means the local overestimation by S1 with ca. 7 cm.

It was found that the individual outliers in sea state in TS-X SM are connected to large slick-looking structures mostly due to algae bloom, oil, etc., which depict a stronger NRCS contrast in X-band (TS-X) in comparison to C-band (S1) ("dark spots" with low NRCS). These cover multiple subscenes and therefore cannot be correctly filtered out in the subscene-preparation and control-of-feature processing steps. It was found that generally, in S1 IW C-band scenes (with a lower spatial resolution), these local slicks are not so strongly pronounced.

A cross-comparison for collocated S1 IW, TS-X and buoys were carried out and shown in Fig. 13. The cross-comparison matrix presents RMSEs for each combination for all four sources including model is presented. Unfortunately, such quadruple collocations are very rare ($N = 152$ means number of all S1 IW subscenes collocated to TS-X subscenes and also collocated to a buoy). Statistically it can be only summarized that RMSE values are on the same order as the uncertainties for each equipment.

B. Technical Implementation for Daily NRT Services

The current version of the SSP is integrated into the S1 NRT processing chain which is part of Copernicus Collaborative Ground Segment developed by the Maritime Safety and Security Laboratory at the German Remote Sensing Data Center (DFD) GS in Neustrelitz (NZ) [28], [29]. For the SSP, the data acquired daily over the North and Baltic Seas are processed directly and the derived information products are delivered to users in NRT.

The GS in Neustrelitz is located north of Berlin at 53°19.779′N, 13°4.247′E and thus offers ideal opportunities to receive and process satellite data acquired over Europe in the so-called "direct downlink (Pass Through) mode." Fig. 9 shows the 5° reception mask of GS NZ which represents the area of possible direct downlink acquisitions. For S1 reception, DLR's Front End Processor (FEP) is in use to generate the Level-0 (L0) products and is configured to consider only Pass Through (VC37–VC44) and NRT (VC4–VC19) data packages.

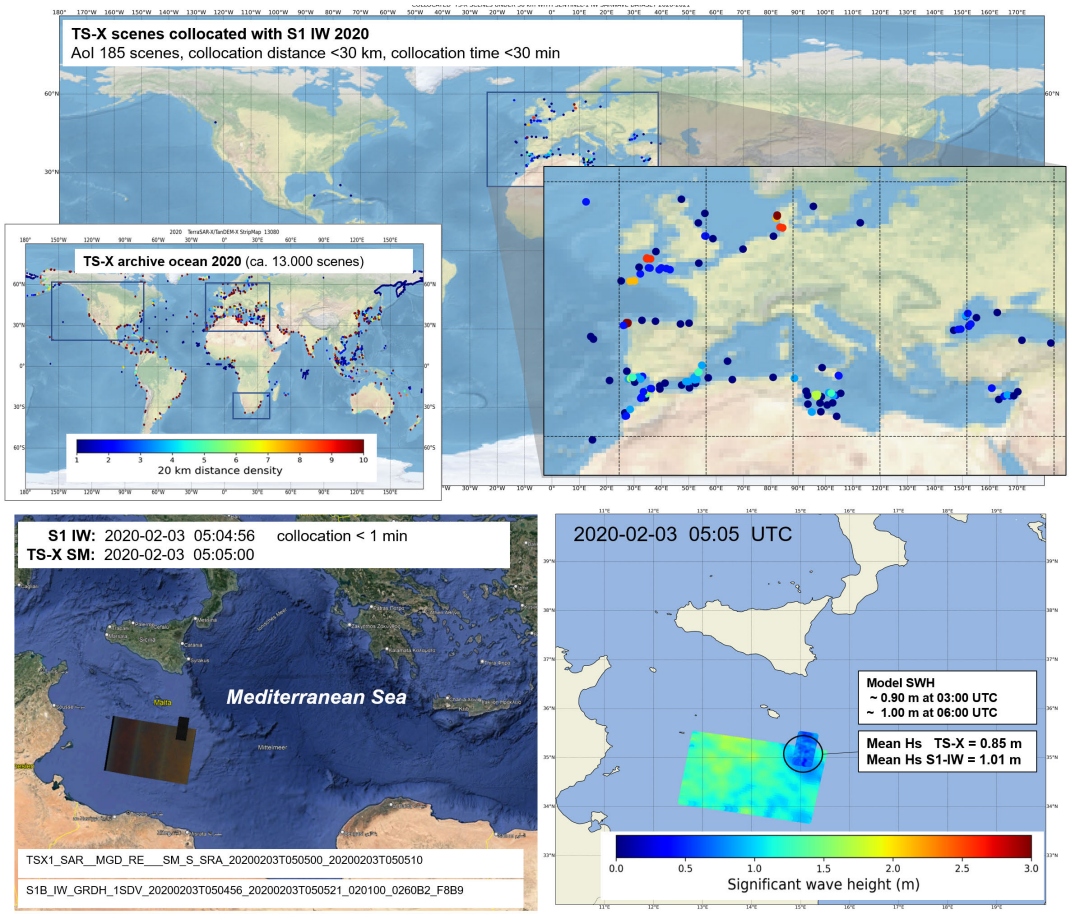

Fig. 7. TS-X SM scenes from the TS-X SM ocean archive 2020 collocated with S1 IW scenes collected in scope of SARWAVE study (AoI, ca. 12.000 scenes, Fig. 3) with 30 km and 30 min (first row, the whole ocean archive displayed bottom left), the color means scenes density within 20 km considering TS-X SM scene centers. An example of a direct collocation between S1 IW and TS-X SM (second row) with a rare collocation of under 1 min.

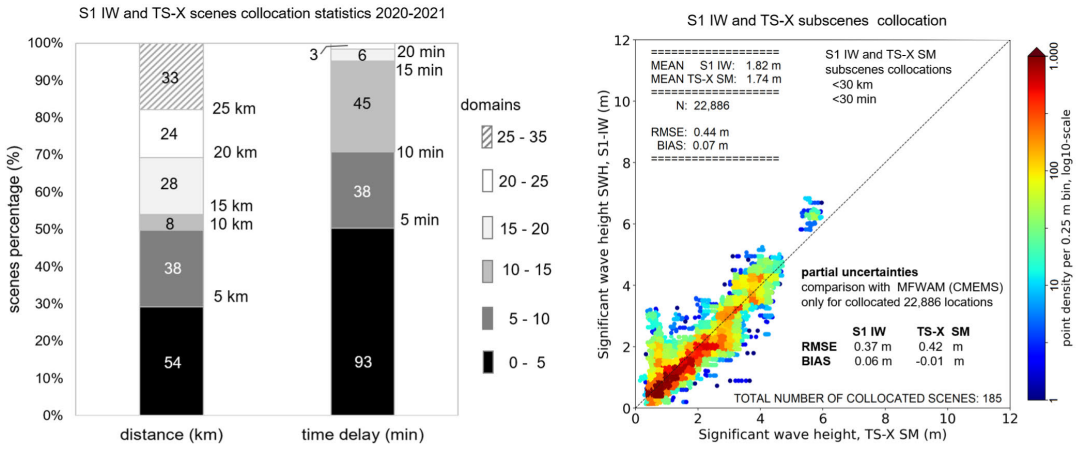

Fig. 8. (Left) Collocation of S1 IW (see Fig. 3) and TS-X SM scenes for 2020 and 2021. The statistic for collocation in time and space is given independently with dividing the data into six domains. The bars show both: the number of scenes (inside bars) for each domain and cumulative percentage of the collocated images. (Right) Scatterplot for collocated subscenes; one value in S1 IW (5 km raster processing step) corresponds to a series of H_s from TS-X (1.5 km raster) in 30 km circle around center of S1 IW subscene. The RMSE = 0.44 m corresponds to total RMSE of S1 IW. The BIAS = 0.07 m shows a slight local overestimation of S1 for collocated cases by comparison with model for these near-coastal locations.

Once the first L0 slice product (SAFE format) is completed, the Telemetry Processing Unit (TM Proc) generates a transfer request for the distribution unit, which immediately starts the transfer to the image and value-adding processing system.

The Instrument Processing Facility (IPF) developed for the ESA Payload Data Core Ground Segment (PDGS) is used to generate Level 1 (L1) products. The IPF was developed by MacDonald, Dettwilerand Associates Ltd. (MDA), Canada,

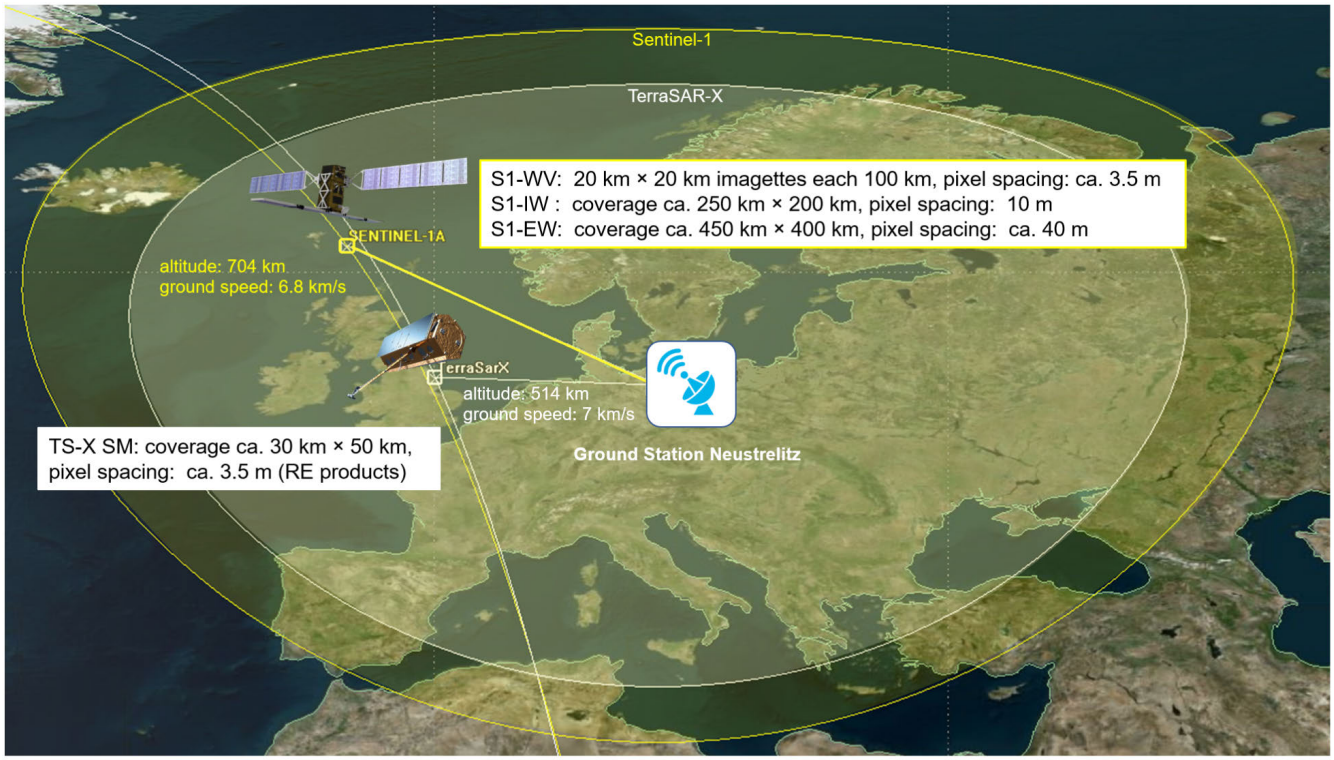

Fig. 9. GS Neustrelitz and acquisition circles for S1 and TS-X satellites, 5° elevation. Inside of the yellow acquisition circles the data can be transferred from satellites to GS directly after acquisition for Near-Real-Time processing. Text boxes present the parameters of satellite modes included into current version of SAR-SeaStaR.

under contract of ESA and was also licensed and supported for the collaborative ground segment. The solution implemented for the NRT processing framework is based on the Processing System Management (PSM), which provides a systematic process flow and also controls subsequent Level-2 (L2) processing.

The SSP is part of SAINT, developed at the DLR Maritime Safety and Security Laboratory Bremen. It is provided as a container, enabling easy integration into the PSM. Subscription rules allow user requests to be directly linked to on-demand GS planning and L2 processing.

L2 products with meteo-marine parameters (sea state and wind fields) are typically delivered within 15 min after acquisition. This is accomplished using standard methods such as FTP, SFTP, Google storage, and rapid delivery via e-mail or web mapping servers. Fig. 10 shows an example result of the SSP visualized in the Maritime Surveillance System (MARISS) Web Client, which was developed at the DLR Maritime Safety and Security Laboratory Neustrelitz.

C. Application for Arctic Under Partial Ice Coverage

The method was applied for studies of sea state in the Arctic. All archive TS-X SM scenes acquired over the Canadian coast in an area north of 68° latitude around Herschel Island (north of Alaska) for summer periods (175 partially ice-free scenes found) were processed in scope of a study [30] to assess the bottom shear stress which triggers erosion and were validated against the hindcast model [21]. Although the acquisitions with high percentages of ice and ice floes in many scenes were difficult for processing, the filtering and control-of-features procedures allowed to detect the largest proportion of ice-spoiled subscenes as "non-valid" and reach a total accuracy of 0.37 m for H_s. This is only 2 cm below the overall accuracy of the TS-X SM reported in the study conducted in ice-free zones south of 60° latitude. It is noteworthy that the majority of the ice-covered subscenes were automatically recognized as "nonvalid" by control features (E_r in the first place, more information on control features can be found in [14]) and ice floes are treated successfully as ships, where NRCS-outlier pixels in a subscene are replaced by the subscene NRCS mean value.

V. Summary

A. Method Generally and Cross Comparisons for Different Satellites

In the scope of this study, a new method was developed allowing the estimation of a series of sea state parameters in the form of fields for multiple satellites/modes in near-real time with improved accuracy for the significant wave height H_s and the second moment wave period T_{m2}. By comparison with models, in terms of H_s, an RMSE = 0.42 m for S1 IW, RMSE = 0.51 m for S1 EW and RMSE = 0.35 m for TS-X SM were reached. In terms of T_{m2}, an RMSE = 0.88 s for S1 IW, RMSE = 0.69 s for S1 EW, and RMSE = 0.45 s for TS-X SM were achieved. The advantage of the method is its applicability not only for open ocean with well pronounced long swell but also for coastal areas with short windsea and for calm wind conditions. The method does not depend on

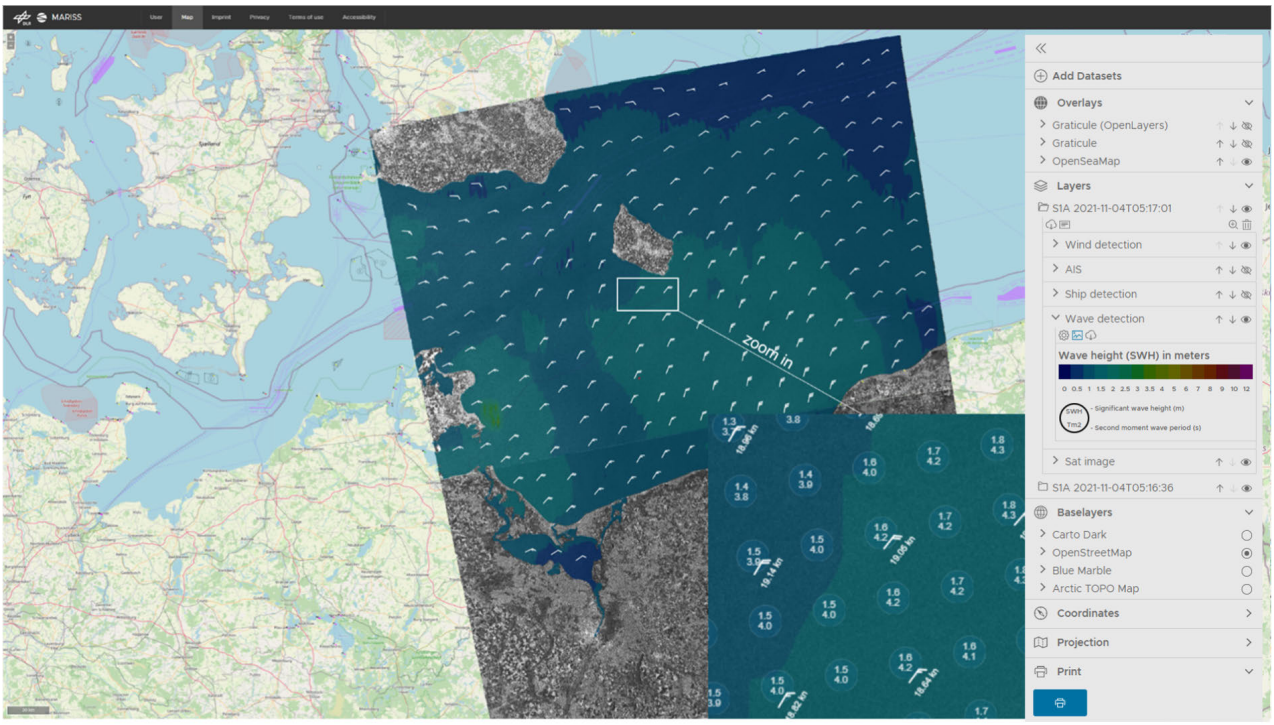

Fig. 10. Demonstrator for NRT services at GS Neustrelitz with implemented SAINT&SAR-SeaStar. The demonstrator runs daily for S1 IW in Southern North Sea and Western Baltic Sea. The processing raster is 3 km, the wave-detection layer shows wave height (background color) and wave period (in circles: H_s top, T_{m2} bottom). Data for eight sea state parameters can be directly downloaded as Google-Earth kmz file. The wind-detection layer (white wind flags) shows the wind speed estimated from the SAR image.

the *cut off* which is just one feature in the set of other features. It is also not dependent on type of sea state imaging (linear/nonlinear, wave-looking-structures/noise-only imaged). The accuracy is not dependent on imaging of swell in SAR and is not connected to proportion of swell in total H_s.

For the first time, a comparison for sea state estimated from different satellites with different radar bands and scanning modes was carried out based on an archive processing. It was found that from ca. 12 000 annual TS-X SM ocean scenes ca. 90 can be collocated to S1 IW within 30 km and 30 min. There, ca. 25% of collocations are a direct overlapping and ca. 50% closer than 5 min in time (see Fig. 8). The comparisons of the collocated wave height estimated using the presented method from S1 IW and TS-X SM resulted in an RMSE = 44 cm, which corresponds to the general accuracy of S1 IW of 42 cm, and a BIAS$\sim$7 cm, which means a slow overestimation by S1 for collocated samples located predominantly in coastal waters.

B. Sea State From Different Satellite Modes

It was found that the training for various satellite SAR modes has differences not only due to technical parameters of the acquisition like resolution but also due to differences of acquisition areas by different modes. As S1 acquires WV mode imagettes across the open ocean and generally switches to IW and EW in shelf waters and Polar Regions, the kind of sea state and ground truth uncertainties are different. It was shown that for the WV acquisitions, only sea state with a period T_{m2} >4 s (predominantly includes swell) are imaged. On the other hand, in the IW scenes around 22% of acquisitions have a wave period T_{m2} <4 s. This means waves with short wavelengths are under ca. 50 m (two times under *cutoff*). Such waves are imaged as noise without any wave-looking patterns. Furthermore, ca. 10% of all S1 IW acquisitions worldwide are in wind shadowed areas (e.g., Mediterranean Sea) with winds under 1.5 m $\cdot$ s^{-1}. Under such near-zero wind, no required capillary waves are built, the Bragg radar scattering does not take place and only specular noise from the sea surface can be used for estimations (for open ocean WV mode, winds under 1.5 m $\cdot$ s^{-1} are only ca. 1%).

C. Method Development

It was shown that the method designed and trained for near-real-time application under all conditions can process all data without excluding "nonvalid" scenes (e.g., homogeneity test, low wind) without loss of accuracy. In the study, only individual subscenes ("black gaps" with zero NRCS due to invalid pixels by row SAR data processing, multiple ships in one subscene, wind turbines, oils spills, or sea ice floes) were detected as "error" with ca. 0.1% of all data (subscenes).

The processing of the large archives of many thousand scenes shows that it is not realistic to completely remove and correct all artifacts and ambiguities in SAR images. Outliers in the results are inevitable if only the model function is applied. However, the results of the model functions, developed for different parameters independently, can be subsequently improved by connection of the resulting parameters. A series of thresholds and filters based on parameter definitions (e.g., $H_s > H_s^{\text{swell}-1} > H_s^{\text{swell}-2}$, $H_s > H_s^{\text{wind}}$) and wave energy conversation (sum of squares of three components

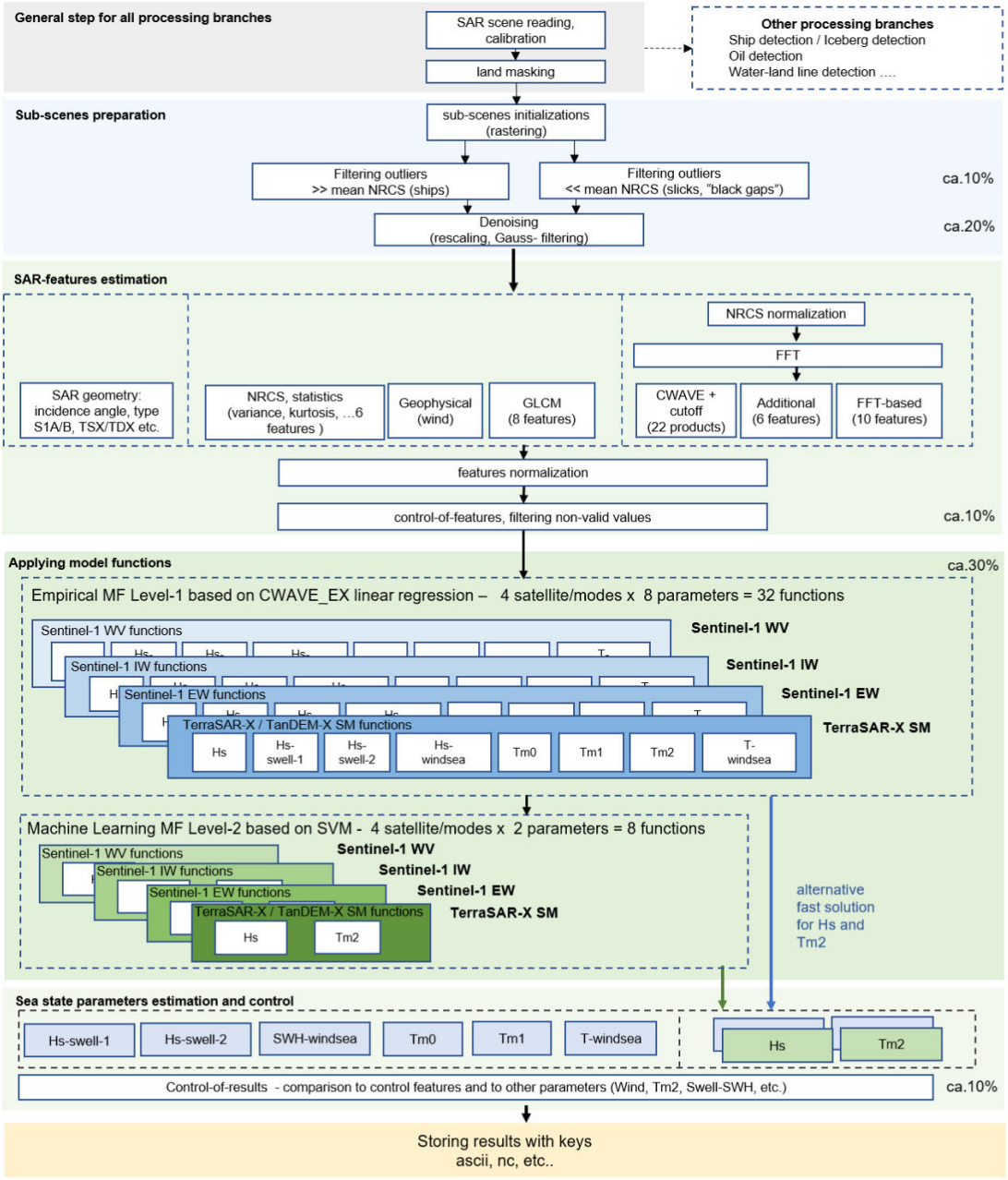

Fig. 11. SAR-SeaStaR algorithm workflow realized in SSP as a part of SAINT package for processing meteo-marine information, targets, and processes at sea surface from SAR imagery. The current version of the algorithm includes 32 CWAVE_EX model functions (four satellite/modes, eight sea state parameters) and eight SVM ML functions (four satellite/modes H_s and T_{m2}). For each processing operation, the approximate effects in percent on resulting RMSE in terms of wave height are shown on the right; for the model functions, this is compared to CWAVE method [11].

dominant and secondary swells and windsea) were implemented. Furthermore, from statistics and measurements, the connections between wave height, wind, and wave period were implemented (details in Section II-G "Additional correction and filtering procedures") in control-of-results filters. All these filters contribute to a significant reduction of the percentage of outliers.

The processing and validation of the large satellite scene archives show, for a competitive accuracy, a state-of-the-art algorithm, additional to model function, has to include a series of processing steps, each needed to reach high accuracy, deal with outliers in the results, and must be adopted for each satellite/mode. It was found that, independent of satellite/mode, even for an accurate ML function, these steps (including the subscene preparation by finding and resetting NRCS outliers, denoising, control of the SAR features, correction of the results by filtering, control of the resulting sea state parameters) contribute to an improvement comparable with the improvement of the ML model to the LR solution.

D. Trainings

The period T_{m2} was first trained for SAR imagery based on global datasets including open ocean, coastal areas and closed

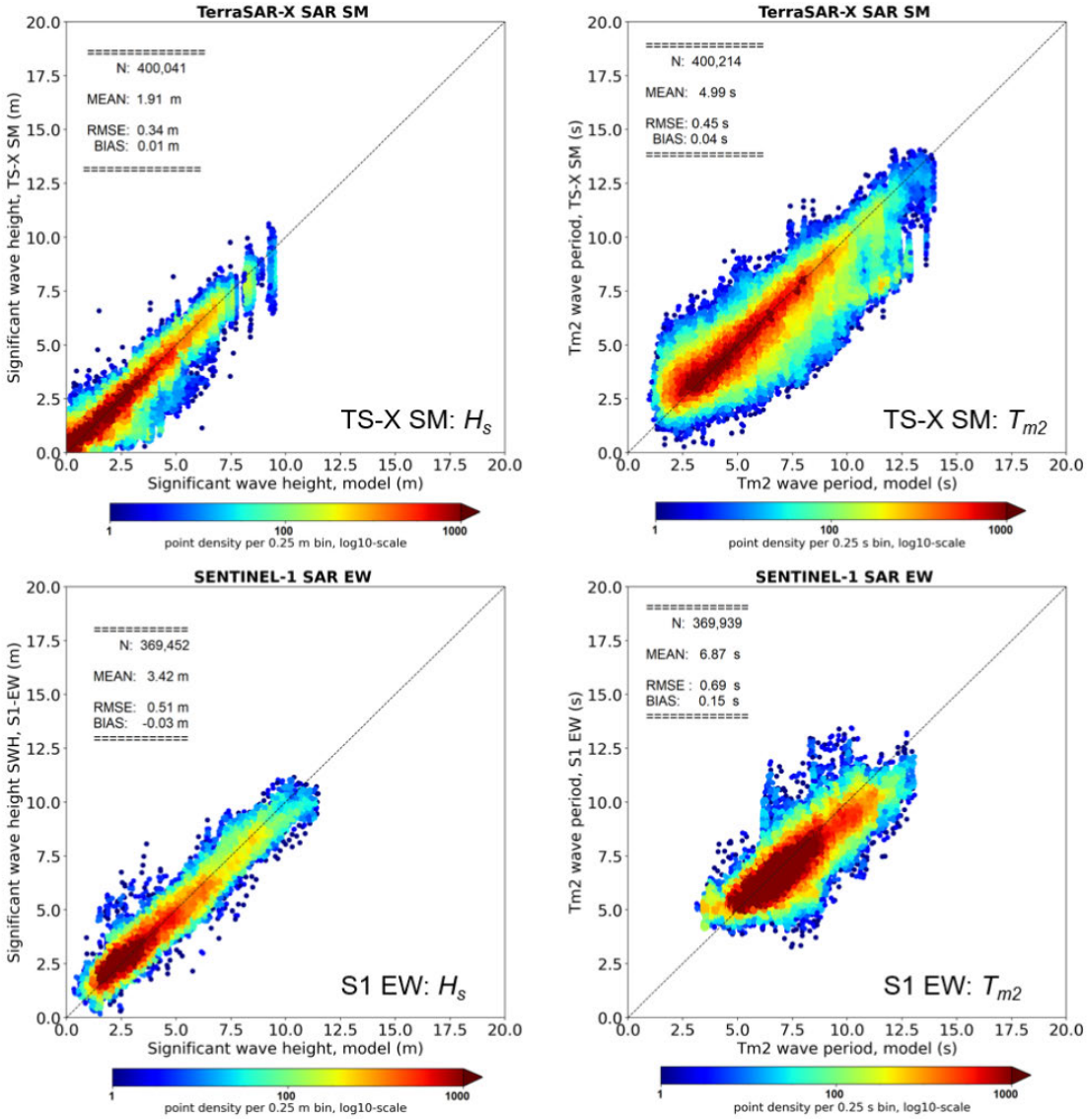

Fig. 12. Validations for TS-X SM and S1 EW for significant wave height H_s and T_{m2} wave period. In the 30 × 50 km TS-X 1.5 km raster results, the local distribution by comparison to coarse model grid points 1/12°. S1 EW with ca. 400 × 450 km processed with a raster of 20 km corresponds to ca. each second model grid point. TS-X SM are dominantly acquired over coasts with basically lower sea state (mean $H_s \sim 2$ m, $T_{m2} \sim 5$ s), while the largest part of S1 EWs are acquired in North Atlantics (mean $H_s \sim 3.5$ m, $T_{m2} \sim 7$ s).

seas with an accuracy in the order of 0.8 s. It was found that training the wave periods needs much more capacity than the wave height, especially due to areas with very low sea state and wind, which, however, can have very long waves (e.g., in the Mediterranean Sea the areas between islands with mountains).

A phenomenon regarding the trainings of ML models became apparent when validating large datasets. By processing the archives and comparison with ground truth, it was observed that while LR has generally lower accuracy in terms of RMSE in comparison to ML, under rare extreme storm conditions with H_s >8 m (statistically under 1% of all data) the ML can result in a significant error in order of 4–6 m, while LR extrapolates with an error in the order of 2–3 m. This effect is eventually connected to higher flexibility of ML functions, which need larger datasets for different domains, in comparison to LR. It was found that a difference between H_s estimated by ML and LR of more than 4 m indicates a failure of SVM ML (outlier), where the resulting H_s is reset to the LR solution CWAVE_EX.

E. Technical Note and Application

The complete method was made operational with direct processing of all data using ML models, while in the previous study [14], ML was only applied for S1 WV H_s as an additional postprocessing procedure. The additional advantage of the developed algorithm and processor is the possibility to switch between SVM functions or replace them with updated ones developed using an extended training dataset. This creates the opportunity to continuously improve the processed results for different parameters of the complete system.

The processing of the archives extends the available data and enables new applications for estimating the parameters connected to local sea state. For example, in [36], the method

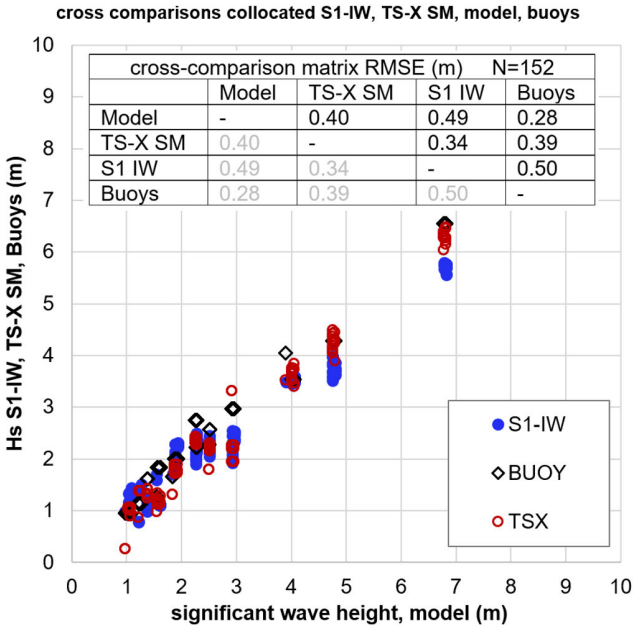

Fig. 13. Cross-comparison for quadruple collocations S1 IW, TS-X, buoys and model for 2020 and 2021 archived data. The RMSE cross-comparison matrix for all four sources. The partial RMSEs are calculated only for locations where all four sources are available.

was applied to process sea state in shelf waters around USA and Canada; all S1 IW in 2015–2020 covering the NDBC buoys provide sea state measurements, ca. 10 000 scenes, were processed and validated with model and buoys. That study confirms the RMSE numbers estimated in this work and uses, for the first time, the local sea state variations for retrieving the roughness length of the sea surface.

The application of the method by processing TS-X SM in the Arctic (Herschel Island north of Alaska, ca. 69° latitude, 175 scenes in archive) with partial ice coverage shows the total accuracy of 0.37 m for H_s [30] by comparison to the hindcast model results MFWAM. This is only 2 cm below the RMSE for TS-X SM reported in the study conducted in ice-free zones south of 60° latitude.

The potential to process a series of sea state parameters including partial integrated such as dominant and secondary swell and windsea allows connecting the empirical methods to wave spectra estimation methods based on transfer functions (e.g., [31], [32], [33]). A joint product could be an opportunity to improve both methods and contribute to forecast modeling where the wave spectra from remote sensing are assimilated (e.g., [34], [35]).

APPENDIX

The algorithm SAR-SeaStaR includes the complete processing chain with a series of steps each needed to reach high accuracy (see Fig. 11). The basic processing runs with CWAVE_EX LR models, for H_s and T_{m2} the ML models are available.

REFERENCES

[1] S. Voinov, E. Schwarz, D. Krause, and B. Tings, "Earth observation maritime surveillance system," in *Proc. GeoForum MV*, Sep. 2020, pp. 73–77.

[2] E. Schwarz, D. Krause, M. Berg, H. Daedelow, and H. Maas, "Near real time applications for maritime situational awareness," in *Proc. 36th Int. Symp. Remote Sens. Environ., Remote Sens. Spatial Inf. Sci.*, Berlin, Germany, 2015, p. 6.

[3] A. L. Pleskachevsky, W. Rosenthal, and S. Lehner, "Meteo-marine parameters for highly variable environment in coastal regions from satellite radar images," *ISPRS J. Photogramm. Remote Sens.*, vol. 119, pp. 464–484, Sep. 2016.

[4] A. Pleskachevsky, S. Jacobsen, B. Tings, and E. Schwarz, "Estimation of sea state from Sentinel-1 synthetic aperture radar imagery for maritime situation awareness," *Int. J. Remote Sens.*, vol. 40, no. 11, pp. 4104–4142, Jun. 2019.

[5] B. Tings, A. Pleskachevsky, D. Velotto, and S. Jacobsen, "Extension of ship wake detectability model for non-linear influences of parameters using satellite based X-band synthetic aperture radar," *Remote Sens.*, vol. 11, no. 5, p. 563, Mar. 2019.

[6] S. Singha, M. Vespe, and O. Trieschmann, "Automatic synthetic aperture radar based oil spill detection and performance estimation via a semi-automatic operational service benchmark," *Mar. Pollut. Bull.*, vol. 73, no. 1, pp. 199–209, Aug. 2013.

[7] A. Frost, S. Wiehle, S. Singha, and D. Krause, "Sea ice motion tracking from near real time SAR data acquired during Antarctic circumnavigation expedition," in *Proc. IEEE Int. Geosci. Remote Sens. Symp. (IGARSS)*, Jul. 2018, pp. 2338–2341.

[8] B. Tings, "Non-linear modeling of detectability of ship wake components in dependency to influencing parameters using spaceborne X-band SAR," *Remote Sens.*, vol. 13, no. 2, p. 165, Jan. 2021.

[9] B. Tings, A. Pleskachevsky, and S. Wiehle, "Comparison of detectability of ship wake components between C-band and X-band synthetic aperture radar sensors operating under different slant ranges," *ISPRS J. Photogramm. Remote Sens.*, vol. 196, pp. 306–324, Feb. 2023.

[10] M. Bruck, "Sea State measurements using TerraSAR-X/TanDEM-X data," Ph.D. theses, Fac. Math. Natural Sci., Univ. Kiel, Kiel, Germany, 2015.

[11] J. Schulz-Stellenfleth, T. König, and S. Lehner, "An empirical approach for the retrieval of integral ocean wave parameters from synthetic aperture radar data," *J. Geophys. Res., Oceans*, vol. 112, no. C3, p. 14, 2007.

[12] J. E. Stopa and A. Mouche, "Significant wave heights from Sentinel-1 SAR: Validation and applications," *J. Geophys. Res., Oceans*, vol. 122, no. 3, pp. 1827–1848, Mar. 2017.

[13] B. Quach, Y. Glaser, J. E. Stopa, A. A. Mouche, and P. Sadowski, "Deep learning for predicting significant wave height from synthetic aperture radar," *IEEE Trans. Geosci. Remote Sens.*, vol. 59, no. 3, pp. 1859–1867, Mar. 2021, doi: 10.1109/TGRS.2020.3003839.

[14] A. Pleskachevsky, B. Tings, S. Wiehle, J. Imber, and S. Jacobsen, "Multiparametric sea state fields from synthetic aperture radar for maritime situational awareness," *Remote Sens. Environ.*, vol. 280, Oct. 2022, Art. no. 113200.

[15] S. Wiehle, S. Mandapati, D. Günzel, H. Breit, and U. Balss, "Synthetic aperture radar image formation and processing on an MPSoC," *IEEE Trans. Geosci. Remote Sens.*, vol. 60, pp. 1–14, 2022.

[16] H. Hersbach, "CMOD5.N: A C-band geophysical model function for equivalent neutral wind," ECMWF, Tech. Rep., 2008.

[17] X.-M. Li and S. Lehner, "Algorithm for sea surface wind retrieval from TerraSAR-X and TanDEM-X data," *IEEE Trans. Geosci. Remote Sens.*, vol. 52, no. 5, pp. 2928–2939, May 2014.

[18] C.-C. Chang and C.-J. Lin, "Training υ-support vector regression: Theory and algorithms," *Neural Comput.*, vol. 14, no. 8, pp. 1959–1977, Aug. 2002.

[19] Z. Wen, J. Shi, Q. Li, B. He, and J. Chen, "ThunderSVM: A fast SVM library on GPUs and CPUs," *J. Mach. Learn. Res.*, vol. 19, no. 21, p. 16, 2018.

[20] ESA. (2017). *ESA News: Sentinel-1 Sees Through Hurricanes*. [Online]. Available: http://www.esa.int/Our_Activities/Observing_the_Earth/Copernicus/Sentinel-1/Sentinel-1_sees_through_hurricanes

[21] F. Ardhuin et al., "Semi-empirical dissipation source functions for wind-wave models: Part I, definition, calibration and validation at global scales," *J. Phys. Oceanogr.*, vol. 40, pp. 1917–1941, Jan. 2010.

[22] CMEMS. *Copernicus Marine Environment Monitoring Service*. Accessed: Jun. 2024. [Online]. Available: https://marine.copernicus.eu/

[23] *NOAA*. Accessed: Jul. 2024. [Online]. Available: https://polar.ncep.noaa.gov/waves/

[24] *NDBC*. Accessed: Jul. 2024. [Online]. Available: https://www.ndbc.noaa.gov/

[25] *ECCC*. Accessed: Dec. 2023. [Online]. Available: http://www.meds-sdmm.dfo-mpo.gc.ca/isdm-gdsi/waves-vagues/index-eng.htm
[26] *EMODnet*. Accessed: Jun. 2024. [Online]. Available: http://www.emodnet-physics.eu/Map/#
[27] *SARWAVE*. Accessed: Jul. 2024. [Online]. Available: http://www.sarwave.org
[28] *Sentinel-1 Instrument Processing Facility Interface Control Document, Issue/Revision 1/9*, Standard S1-IC-MDA-52-7454 Sep. 2015.
[29] D. Krause, E. Schwarz, S. Voinov, H. Daedelow, and D. Tomecki, "Sentinel-1 near real-time application for maritime situational awareness," *CEAS Space J.*, vol. 11, pp. 45–53, Jun. 2018.
[30] K. Brembach, A. Pleskachevsky, and H. Lantuit, "Investigating high-resolution spatial wave patterns on the Canadian Beaufort shelf using synthetic aperture radar imagery at Herschel island, Qikiqtaruk, Yukon, Canada," *Remote Sens.*, vol. 15, no. 19, p. 4753, Sep. 2023.
[31] W. Alpers and C. Rufenach, "The effect of orbital motions on synthetic aperture radar imagery of ocean waves," *IEEE Trans. Antennas Propag.*, vol. AP-27, no. 5, pp. 685–690, Sep. 1979, doi: 10.1109/TAP.1979.1142163.
[32] S. Hasselmann, C. Brüning, K. Hasselmann, and P. Heimbach, "An improved algorithm for the retrieval of ocean wave spectra from synthetic aperture radar image spectra," *J. Geophys. Res., Oceans*, vol. 101, no. 7, pp. 16615–16629, 1996.
[33] H. Wang et al., "Quantifying uncertainties in the partitioned swell heights observed from CFOSAT SWIM and Sentinel-1 SAR via triple collocation," *IEEE Trans. Geosci. Remote Sens.*, vol. 60, pp. 1–16, 2022.
[34] S. Abdalla, J. R. Bidlot, and P. Janssen, "Global validation and assimilation of ENVISAT ASAR wave mode spectra," in *Proc. SeaSAR*, vol. 613. Frascati, Italy, Jan. 2006, p. 6.
[35] S. Abdalla, J. Bidlot, and P. Janssen, "Envisat ASAR wave mode spectra global validation and assimilation," in *Proc. SeaSAR*, Frascati, Italy, vol. 679, Jan. 2010, pp. 25–29.
[36] A. Owda, A. Pleskachevsky, X. Guo Larsén, M. Badger, D. Cavar, and C. Bay Hasager, "Evaluation of SAR-based sea state parameters and roughness length derivation over the coastal seas of the USA," *IEEE J. Sel. Topics Appl. Earth Observ. Remote Sens.*, vol. 17, pp. 9415–9428, 2024.

Andrey Pleskachevsky received the Diploma degree in hydropower engineering from Technical University at St. Petersburg, St. Petersburg, Russia, in 1994, with focus on hydrodynamic numerical modeling and data analyses, and the Ph.D. degree from GKSS-Research Center (now Helmholtz Center HERION), Geesthacht, Germany, in 2009, working on spectral wave modeling and coupling of waves, circulation and suspended matter transport models, and implementation of satellite data into modeling.

In 2009, he joined the Remote Sensing Technology Institute, German Aerospace Center (DLR), Bremen, Germany, where he developed algorithms for retrieval of the meteo-marine parameters from synthetic aperture radar for near-real-time services.

Björn Tings received the dual bachelor's degree in scientific programming and in mathematical-technical software development from FH Aachen, Aachen, Germany, and RWTH Aachen University, Germany, in 2010, respectively, and the master's degree in artificial intelligence from Maastricht University, Maastricht, The Netherlands, in 2013.

Since 2013, he has been a Research Associate in the team of SAR-oceanography at the Remote Sensing Technology Institute, German Aerospace Center (DLR), Bremen, Germany. His research interests include the automatic detection and classification of ship signatures on SAR imagery.

Sven Jacobsen received the Diploma degree in geophysics from the Institute of Geophysics and Meteorology, University of Cologne, Germany, in 2007, and the Ph.D. degree in space plasma physics and fluid dynamics from the Institute of Geophysics and Meteorology, University of Cologne, in 2011.

Since 2011, he has been working in the area of oceanography and remote sensing. In 2013, he joined DLR and became The Head of the Maritime Safety and Security Center at Bremen, Bremen, Germany, in 2016. He and his team work on the development of software algorithms to derive maritime information (wind fields, sea state, oil-, ship-, and ice-berg detection, etc.) from satellite data.

Stefan Wiehle received the Diploma degree in physics and the Dr.rer.nat. degree from Technical University Braunschweig, Braunschweig, Germany, in 2010 and 2014, respectively.

He works at the DLR Maritime Safety and Security Laboratory at Bremen, Bremen, Germany, a group at DLR's Remote Sensing Technology Institute (IMF). He also led DLR's activities in several research projects. His research interests include the implementation and automation of SAR maritime value-adding algorithms such as land-water-line detection, bathymetry derivation, or sea ice classification.

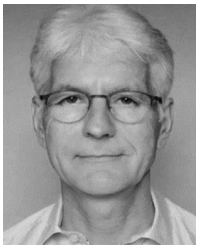

Egbert Schwarz has received the Diploma (Dipl.Ing.) degree in electrical engineering from the School of Engineering Dresden, in 1990.

He is currently leading the Maritime Safety and Security Laboratory at Neustrelitz, Neustrelitz, Germany, and the Team Leader of the remote sensing team Maritime Security. The work is carried out in the context of assuring safe shipping, protecting oceans and coastal waters, and supporting public authorities in their efforts to combat activities like ocean dumping of hazardous material, illegal fishery, and search and rescue. In 2002, he began working at the German Remote Sensing Data Center (DFD), part of the Earth Observation Center (EOC) of the German Aerospace Center (DLR), Neustrelitz. In the "National Ground Segment" Department in Neustrelitz, he was a Group Leader of the "Real-Time Processing" team since 2009, responsible for service development, station operation, and real-time processing. His research interests include systems engineering and the development of thematic real-time remote sensing applications for maritime situational awareness.

Detmar Krause received the Engineering degree (Dipl.Ing.) in automation technologies from the University of Applied Sciences Lueneburg, Lueneburg, Germany, in 2000, and the degree in vocational education from the Technical University of Berlin, Berlin, Germany, in 2006.

From 2001 to 2012, he was a Software Trainer and Developer in the Earth Observation team of a private company. Since 2013, he has been working for the DLR as a Scientific Assistant at the Maritime Safety and Security Laboratory at Neustrelitz, Neustrelitz, Germany, and is responsible for fully/half-automated processing systems.